Markerless rat head motion tracking using structured light for brain PET imaging of unrestrained awake small animals

Markerless rat head motion tracking using structured light for brain PET imaging of unrestrained awake small animals

Alan Miranda[1], Steven Staelens[1] Sigrid Stroobants[1, 2] and Jeroen Verhaeghe[1]

[1]Molecular Imaging Center Antwerp, University of Antwerp, Universiteitsplein 1, 2610 Antwerp, Belgium
[2]University Hospital Antwerp, Wilrijkstraat 10, 2650 Antwerp, Belgium

Alan Miranda: alan.mirandamenchaca@uantwerpen.be
Steven Staelens: steven.staelens@uantwerpen.be
Sigrid Stroobants: sigrid.stroobants@uza.be
Jeroen Verhaeghe: jeroen.verhaeghe@uantwerpen.be

Abstract

Preclinical positron emission tomography (PET) imaging in small animals is generally performed under anesthesia to immobilize the animal during scanning. More recently, for rat brain PET studies, methods to perform scans of unrestrained awake rats are being developed in order to avoid the unwanted effects of anesthesia on the brain response. Here, we investigate the use of a projected structure stereo camera to track the motion of the rat head during the PET scan. The motion information is then used to correct the PET data. The stereo camera calculates a 3D point cloud representation of the scene and the tracking is performed by point cloud matching using the iterative closest point algorithm. The main advantage of the proposed motion tracking is that no intervention, e.g. for marker attachment, is needed. A manually moved microDerenzo phantom experiment and 3 awake rat [^{18}F]FDG experiments were performed to evaluate the proposed tracking method. The tracking accuracy was 0.33 mm rms. After motion correction image reconstruction, the microDerenzo phantom was recovered albeit with some loss of resolution. The reconstructed FWHM of the 2.5 and 3 mm rods increased with 0.94 and 0.51 mm respectively in comparison with the motion-free case. In the rat experiments, the average tracking success rate was 64.7%. The correlation of relative brain regional [^{18}F]FDG uptake between the anesthesia and awake scan reconstructions was increased from on average 0.291 (not significant) before correction to 0.909 (p<0.0001) after motion correction. Markerless motion tracking using structured light can be successfully used for tracking of the rat head for motion correction in awake rat PET scans.

Keywords: positron emission tomography, small animal PET, motion correction, markerless motion tracking

1 Introduction

Preclinical positron emission tomography (PET) is used to investigate physiological and biochemical processes in living subjects. PET studies must be performed in the absence of motion to avoid artifacts, such as image blurring, in the reconstructed images. In preclinical PET imaging immobilization of the animal is achieved using anesthesia. Particularly for rat brain studies, it has been shown that the use of anesthesia can be a confounding factor for the neurological process under study (Momosaki *et al.*, 2004; Matsumura *et al.*, 2003; Fueger *et al.*, 2006; Hildebrandt *et al.*, 2008). Awake scans of restrained rats have been performed to avoid the use of anesthesia. However it has been shown that the stress associated with the restraining influences the neurological process of the rat as well (Sung *et al.*, 2009; Patel *et al.*, 2008).

To avoid the unwanted effects of the anesthesia or the induced stress on the neurological response of the rat, methods to perform PET studies of awake and unrestrained rats have been developed by several research groups. One of the approaches is to use specially designed PET detectors attached to the rat head or implanted inside the rat brain (Woody *et al.*, 2007; Schulz *et al.*, 2011; Balasse *et al.*, 2015). These methods require special hardware and surgical intervention. These system have been used to demonstrate the significant impact of anesthesia on [^{11}C]raclopride imaging. However, these approaches suffer from low spatial resolution and low sensitivity in comparison with state of the art preclinical PET.

A second approach is to use commercially available preclinical PET scanners and to track the motion of the rat head during the scan so that the PET data can be corrected for the measured motion (Menke *et al.*, 1996). Several approaches have been used to track the motion of the rat head during the PET scan. Most often an optical stereo camera tracking the motion of a checkerboard marker that is rigidly attached to the rat head has been used (Zhou *et al.*, 2008; Kyme *et al.*, 2011). The submillimeter tracking accuracy of this method is sufficient to perform motion correction in preclinical PET scanners. Nevertheless, the marker is prone to slip on the rat head or to be detached by the rat during the PET scan. Markerless motion tracking relying on natural features of the rat head has also been considered (Kyme *et al.*, 2014). Using four monocular cameras, different views of the rat head are acquired, matching features of the rat head in the different views to obtain 3D information. Due to the limited number of distinct natural features on the rat head, marks have to be painted on the rat head for reliable tracking. Finally, tracking radioactive point sources attached to the rat head have been used to track the rat head during the PET scan (Miranda *et al.*, 2015). With this method no external tracking device is necessary for the motion tracking. However this method might fail for PET tracers that exhibit a high skull uptake, which could interfere with the signal from the point sources.

Here we use a structured light camera for motion tracking. The use of the projected pattern avoids the need for texture information in the 3D scene and is therefore an excellent candidate for markerless tracking of the rat head. Motion tracking using structured light cameras has been implemented in clinical setups for human brain PET imaging. A near infrared video projector has been adapted by Olesen *et al.* (2012) to track the motion of human subjects. A Microsoft Kinect has also been adapted to track the motion of patients in a PET scanner by Noonan *et al.* (2015). However to our knowledge the use of structured light tracking systems has not been investigated in the context of small animal PET imaging.

In this work we validate the use of a commercially available infrared stereo camera with a structured light projector for head motion tracking during awake rat brain PET imaging. The stereo camera captures the 3D representation of the scene which is then further processed to determine the head motion. We have developed and implemented this motion estimation pipeline in C++ using routines from the open source Point Cloud Library (Rusu and Cousins, 2011). Finally the stereo camera and the motion estimation are validated using phantom and *in vivo* experiments.

2 Methods

2.1 PET scanner and optical camera

PET scanning was performed on a Siemens Inveon microPET (Siemens Medical Solutions, Inc., Knoxville, USA). The scanner consists of 25600 lutetium orthosilicate (LSO) crystals with size 1.5 × 1.5 × 1.0 mm arranged in 80 rings, resulting in a scanner axial length of 127 mm and diameter of 161 mm. The scanner bore diameter, i.e. the viewport for the tracking camera, is 120 mm.

The stereo camera used for the motion tracking is an Ensenso N10 (Ensenso GmbH, Freiburg im Breisgau, Germany). The camera has a built-in infrared random point pattern projector which is visible to the infrared stereo camera. The projected infrared pattern allows performing the stereo matching algorithm even on objects without distinctive texture, such as the white fur of a laboratory rat. The built-in stereo matching algorithm results in a 3D point cloud of the world scene. The particular camera model used has a focal length of 6 mm, a minimum and maximum working distance of 230 and 580 mm respectively and uses two 752 × 480 pixels CMOS sensors. The accuracy of the calculated scene depth map (point cloud) depends on the camera focal length and the object to camera distance. At the minimum and maximum working distance the optics blur is 0.544 and 1.39 mm respectively. The optimal working distance is 320 mm, where the optics blur is 0.0814 mm. The depth resolution is also a function of the object to camera distance. At the minimum and maximum working distance the depth resolution is 0.130 and 0.824 mm respectively.

2.2 Motion tracking

2.2.1 Time synchronization

The stereo camera is triggered through its GPIO 12-24 V input port using a square wave signal as input. An Arduino Uno (Arduino SA) microcontroller is used to generate a 31.2 Hz square wave signal (5 V) that determines the tracking frequency. The signal is connected to the PET scanner gate input and coupled to the stereo camera trigger input using an optocoupler. Every minute, the frequency of the square wave signal is slightly increased for 4 periods of the signal with a predefined pattern to enable the synchronization between the camera data and the PET data.

2.2.2 Spatial calibration

The stereo camera reference coordinate system was defined using the geometry of an irregular tetrahedron with edge size of 25 mm (figure 1A). The tetrahedron is pasted on the PET scanner bore such that three of its faces are always visible when tracking an object (figure 2A). The plane normals of the tetrahedron faces are used to calculate the origin (figure 1B) and orientation (figure 1C) of the coordinate system.

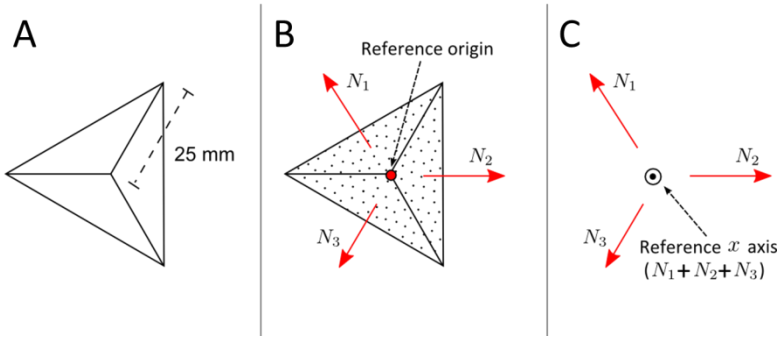

Figure 1. A) Irregular tetrahedron used to calculate the reference coordinate system. B) The normals of the tetrahedron faces (N_1, N_2 and N_3) are calculated to define the planes intersection as the origin of the reference coordinate system. C) The x axis is defined as the sum of all normals ($N_1 + N_2 + N_3$), the y axis as ($N_1 \times x$) and the z axis as ($x \times y$). The order of normals N_1, N_2 and N_3 is defined using the stereo camera coordinate system as reference.

To establish the transformation between the camera reference coordinate system and the PET scanner coordinate system the location of a radioactive point source was measured simultaneously in both the scanner and camera reference coordinate systems at 20 different positions. The transformation matrix

between coordinate systems was then calculated using least squares regression to find the transformation which minimizes the distance between paired measurements. The root mean square error of the transformation was calculated as the average distance between corresponding point sources locations in PET coordinates determined from the PET image and the stereo camera point cloud respectively.

2.2.3 Point cloud processing

Due to the time consuming computations involved in the motion tracking algorithm, the stereo images are recorded together with their calibration information and the motion tracking is performed offline, i.e. processing each frame after the complete acquisition. For instance, for one minute of acquisition the files size was ~750 MB. For the calculation of the scene disparity maps from each pair of stereo images, the manufacturer's Ensenso C++ software development kit (revision 1.3.172) is used (EnsensoGmbH, c2015). The depth map is calculated for each of the 752 × 480 pixels of the image. Pixels with invalid depth values are discarded. The stereo matching algorithm tuning parameters such as the penalty for disparity changes along successive pixels, the shadowing threshold to control how pixels are discarded at the object borders and the uniqueness ratio to filter out unreliable matched pixel values were determined using the stereo images of the PET motion experiments (section 3). The parameters were tuned by examining different parameter values and assessing the noise and outlier level of the resulting point clouds. The parameters that consistently minimize the number of outliers and which did not oversmooth the 3D scene surface were selected as the tuning parameters for all subsequent experiments.

Once the scene point cloud has been calculated, all the remaining processing is performed using the open source C++ Point Cloud Library (version 1.7.2)(Rusu and Cousins, 2011). First, in order to reduce the processing time the scene point cloud is downsampled from an original voxel grid resolution of 0.5 mm to a resolution of 1 mm (figure 2B) by calculating the centroid of the points contained within 1 mm voxels. Then, the points defining the plane of the scanner bore are removed (figure 2C). Therefore, a plane is fitted using the random sample consensus (RANSAC) algorithm (Fischler and Bolles, 1981) to determine the scanner bore plane. Due to the high density of points in the scanner bore plane, the RANSAC algorithm converges rapidly (less than 100 iterations). Once the plane equation has been determined, all the points within an absolute distance of less than 3 mm from the plane are discarded. In this way all scanner bore points were completely removed from the original point cloud image. All subsequent processing is performed on the down sampled point clouds for which the scanner bore was removed.

Before the start of the point cloud tracking procedure, a model of the reference point cloud (tetrahedron detailed in section 2.2.2) and the object to be tracked are created from several point cloud images. To distinguish between the different objects in the point cloud images, a Euclidian clustering is performed (figure 2D). By defining a minimum and maximum cluster size most outlier clusters are removed. The object of interest is then selected manually from the remaining clusters. Due to the fact that often only a partial view of the object is available in each individual frame, the point clouds of several frames with different views are joined in order to build a complete model and to increase its accuracy. The frames with the different views were manually selected from the recording and the point clouds are joined using the iterative closest point (ICP) algorithm (Besl and Mckay, 1992). The combined point cloud is then filtered with a statistical outliers removal (Rusu *et al.*, 2008) and a moving least squares surface reconstruction (Alexa *et al.*, 2003). The resulting model is then edited manually to erase possible remaining outliers and to remove structures that often move independently of the object. In the case of the rat experiments the ears on the rat were removed from the head model.

Finally the eigenvalues of the final point cloud are calculated. We will refer to these eigenvalues as the model eigenvalues.

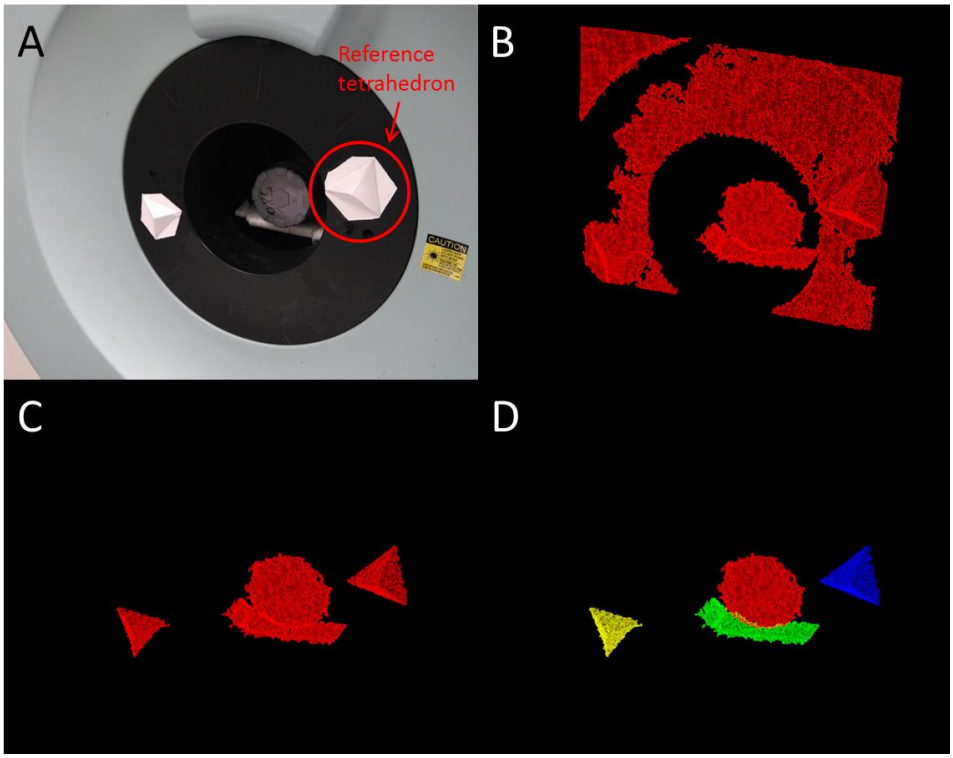

Figure 2. A) Scanner bore (120 mm diameter), reference tetrahedron and object inside the scanner, B) point cloud of the scene in A), C) point cloud after removing scanner bore plane and D) Euclidian clustering of the different objects in the point cloud scene. The smaller tetrahedron was only used for testing and depth alignment of the camera.

Once the model is built for both the rat head and the reference tetrahedron, these objects can be tracked in the point cloud images. For each frame the Euclidian cluster extraction of the scene as described above is performed. The eigenvalues of each point cloud cluster are calculated and their Euclidean distance to the model eigenvalues is determined. The point cloud clusters that match the object and the reference model point clouds the best (i.e. with minimum distance between their eigenvalues and the model eigenvalues) and for which the eigenvalues are within a maximum distance threshold of the model eigenvalues are selected as the matching point clouds in the given frame. Both the object and reference point cloud must be found through the eigenvalue distance calculation to continue with the tracking. Otherwise the tracking in that frame fails. The reference coordinate system position and orientation for the frame is calculated from the tetrahedron geometry of the reference point cloud as described in section 2.2.2. The pose of the rat head is calculated using the ICP algorithm, which finds the rigid spatial transformation (in the camera coordinate system) between the frame object point cloud (source point cloud) and the object model point cloud (target point cloud). To accelerate the pose calculation the initial rigid transformation is initialized to the transformation found in the previous frame. If the tracking in the previous frame was unsuccessful the initial transformation is set to the translation between the centroids of the two point cloud centroids. Once the pose is determined using the ICP algorithm a distance score is calculated as the average of all distances between two corresponding points (as calculated by the ICP algorithm) in the transformed source point cloud and target point cloud respectively. This distance score increases as the overlap between source and target point clouds decreases. A threshold is set to exclude transformations for which the distance

score becomes too large. A maximum distance score threshold of 1.1 mm was used in our experiments.

The calculated pose of the object in the camera coordinate system through ICP is then transformed to the reference coordinate system and then finally to the PET scanner coordinate system.

3 Validation experiments

3.1 Phantom experiment

A microDerenzo phantom with rod sizes of 1.25, 1.5, 2, 2.5 and 3 mm diameter (spacing between rod centers double diameter size), filled with 18.5 MBq of [^{18}F]FDG, was scanned while it was manually moved during 5 minutes. Due to the transparency of the phantom material, the infrared pattern could not be detected on its surface. Therefore, to allow the motion tracking of the phantom, a white opaque marker (asymmetric 4-sided polygon, surface area 30×35 mm) was pasted onto the front of the phantom facing the camera. In addition, a motion-free 5 minutes scan of the phantom was performed for comparison. The motion corrected reconstructions were calculated using motion compensated list-mode ordered subset expectation maximization (OSEM) reconstruction (Rahmim *et al.*, 2004a). The static reconstructions were calculated with list-mode OSEM reconstruction (Rahmim *et al.*, 2004b). Both static and motion corrected reconstructions were performed without attenuation, scatter or randoms correction with 16 subsets and 8 iterations. Reconstructions were implemented in Matlab (The Mathworks, Inc. Natick, United States) using parallelized C libraries for the back and forward projection steps of the list-mode algorithm.

The average speed of the phantom marker was calculated for a point in its centroid, located at 25 mm from the microDerenzo phantom front. To assess the loss of spatial resolution after motion correction, the full width at half maximum (FWHM) of the phantom rods was measured in the motion corrected and motion-free scan reconstructions in the transverse plane. A Gaussian function was fitted to the individual rods and the mean FWHM was calculated for the different rod size groups.

To measure the uncertainty of the motion tracking, the standard deviation in the position and orientation of the static phantom marker as well as that of the reference coordinate system was measured in 300 frames.

3.2 Awake rat brain experiment.

Three female Sprague-Dawley rats (weight 220-295 g, age 11-16 weeks) were scanned awake and under anesthesia. The experiments followed the European Ethics Committee recommendations (decree 86/609/CEE) and were approved by the Animal Experimental Ethical Committee of the University of Antwerp, Antwerp, Belgium (ECD 2016-20). Each rat was injected with 37 MBq of [^{18}F]FDG while under anesthesia (isoflurane in medical oxygen 5% for induction, 2% for maintenance). Immediately after injection anesthesia was stopped and the rat remained awake for a 30 minutes tracer uptake period. Then the rat was placed in a plastic cylindrical container (8 cm inner diameter, 15 cm length) with transparent plastic lids, wherein it could move freely, even turning around. The refraction distortion of the thin plastic lid (0.7 mm thickness) of the projected infrared pattern was assumed to be negligible. Container and rat were placed in the center of the scanner field of view and scanned during 20 minutes while simultaneously recording the scene stereo images for motion tracking. After the awake scan, the rat was anesthetized again (isoflurane in medical oxygen 5% for induction, 2% for maintenance) and scanned for another 20 minutes to acquire a motion-free reference image.

The average speed of the rat head was measured at the centroid of the rat head point cloud (close to the eyes).

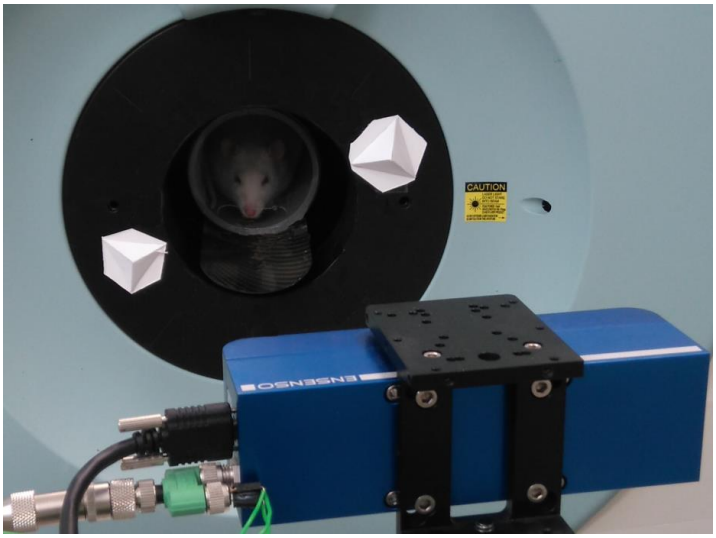

Figure 3. Setup of the rat PET motion correction scan showing the tetrahedron reference on the scanner bore and stereo camera used for the motion tracking.

The awake scan reconstructions, with and without motion correction (same reconstructions as described in section 3.1), were compared to the anesthesia motion-free reconstructions qualitatively and quantitatively by measuring the relative brain FDG uptake (brain uptake normalized to cerebellum uptake) in different regions of the brain. The awake motion corrected reconstructions relative uptake (to cerebellum) should be similar to the anesthesia scan reconstructions relative uptake as the irreversible [^{18}F]FDG tracer reaches a plateau after a 30 min uptake period. After reconstruction, the awake scan image was aligned to the motion-free image through a rigid body transformation. Then, the motion-free and awake scan reconstructions were aligned to an [^{18}F]FDG brain atlas (Schiffer *et al.*, 2006) through a rigid body transformation. The brain atlas is then normalized (elastic registration) to the motion-free reconstructions. Finally, 22 brain regions (averaging left and right symmetric regions) defined in the brain atlas were used to calculate the relative [^{18}F]FDG uptake in these regions from the three images (motion-free (anesthesia), uncorrected (awake) and motion corrected (awake)). The Pearson's correlation coefficient r between anesthesia and awake as well as between anesthesia and awake motion corrected images was calculated for the 3 rats. Finally the Bland-Altman plot, describing the agreement between 2 quantitative measurement through the bias and agreement interval of the difference of the 2 measurements (Giavarina, 2015), was calculated for the anesthesia versus awake and for the anesthesia versus awake motion corrected images relative [^{18}F]FDG uptake combining all 3 rats data. The image analysis was performed in PMOD 3.7 (PMOD technologies Ltd, Zurich, Switzerland).

In addition, to assess the spatial resolution difference in the awake motion corrected reconstructions in comparison with the anesthesia motion-free reconstructions the scale parameter (Babaud *et al.*, 1986) of the motion corrected images was calculated as follows. A mask was defined around the FDG uptake pattern of the brain in the anesthesia image and the awake motion corrected as well as the anesthesia scan images were masked. Then, the anesthesia motion-free reconstruction was filtered with a uniform Gaussian filter with increasing values of the scale parameter σ^2= 0 to 2.88 mm^2. Next, the correlation between the motion corrected reconstructions and the filtered anesthesia reconstructions was

calculated. The scale parameter for which the correlation between these images was maximal was selected as the corresponding scale parameter.

4 Results

4.1 Phantom experiment

The standard deviation of the position and orientation of the tetrahedron (i.e. reference coordinate system) in the camera coordinate system was 0.0394, 0.0334 and 0.0324 mm in the x, y and z directions respectively, and 0.372, 0.0974 and 0.0384 degrees about the x, y and z axis respectively. The root mean square error in the spatial calibration transformation matrix was 0.274 mm.

For the static phantom marker position (measured in the reference coordinate system) the standard deviation in the x, y and z directions was 0.180, 0.216 and 0.180 mm (0.33 mm root mean square) and for the orientation 0.365, 0.820 and 0.716 degrees about the x, y and z axis respectively. The tracking processing time for 9600 frames (5 min of acquisition) was about 100 minutes and the tracking success rate was 79.3%.

The reconstruction of the microDerenzo phantom and a sample of the manual motion applied are shown in figure 4. The average speed throughout the whole scan was 52.8 mm/s.

Table 1 shows the average FWHM for the 2, 2.5 and 3 mm diameter rods in the motion corrected and motion-free reconstructions. After motion correction the structure of the phantom is recovered. However the motion corrected reconstruction suffers from loss of spatial resolution in comparison with the motion-free reconstruction. There is a maximum increase of 0.94 mm in the 2.5 mm rods and a minimum of 0.51 mm in the 3 mm rods.

Table 1. Mean FWHM±std of the 2, 2.5 and 3 mm rods of the microDerenzo phantom in the motion-free scan and motion scan after motion correction.

Rods	2 mm	2.5 mm	3 mm
Motion corrected	2.32 ± 0.08 mm	3.37 ± 0.29 mm	3.34 ± 0.05 mm
Motion-free	1.77 ± 0.11 mm	2.43 ± 0.10 mm	2.83 ± 0.02 mm

4.2 Awake rat brain experiment

Figure 5 shows the head point cloud models for the 3 rats and a sample of the matched point cloud from a single frame. The rat head models were created joining 30 to 50 frames, selected such that the whole head view could be reconstructed. For rat 1, 2 and 3 respectively, the average head speed was 24.4, 17.4 and 22.2 mm/s, the average distance score of the matched head was 1.05, 0.808 and 0.677 mm, and the tracking success rate was 38.5%, 82.6% and 73.1%. The low tracking success rate for rat 1 was caused mostly by the rat turning away from the stereo camera as well as long grooming periods (10 % of the time), adding excessive clutter to the head point cloud.

The reconstruction for the 3 different cases (motion-free, uncorrected and corrected awake scans) are shown in figure 6 for the 3 rats. For the awake scan, after motion correction, FDG brain uptake in regions such as cortex, cerebellum and hippocampus can be identified while these patterns are lost in the uncorrected image.

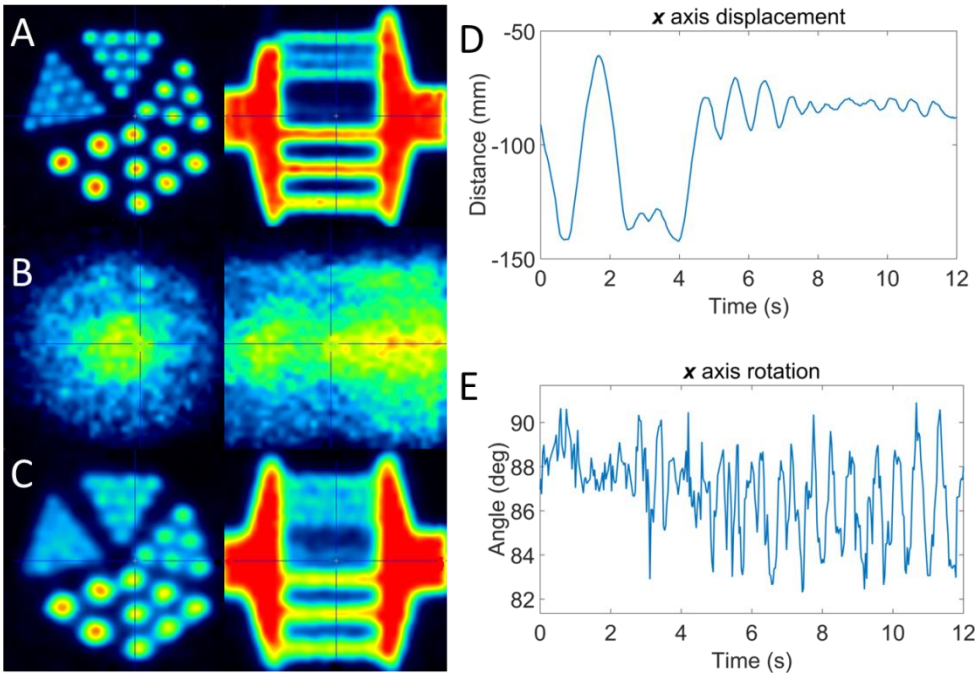

Figure 4. Reconstruction of the microDerenzo phantom with rod diameters 1.25, 1.5, 2, 2.5 and 3 mm A) motion-free scan, B) uncorrected reconstruction of the manually moved scan and C) the corresponding motion corrected reconstruction. D) Displacement along and E) rotation about the x axis of the microDerenzo phantom during 12 seconds of the motion scan.

The correlation coefficient r between the relative [^{18}F]FDG uptake of the anesthesia versus awake scans and the anesthesia versus awake motion corrected images for the 3 rats is shown in Table 2. As expected, for the uncorrected images, there is no or only a weak correlation. After motion correction there is a strong (r >0.88) and significant (p<0.0001) correlation for all 3 cases.

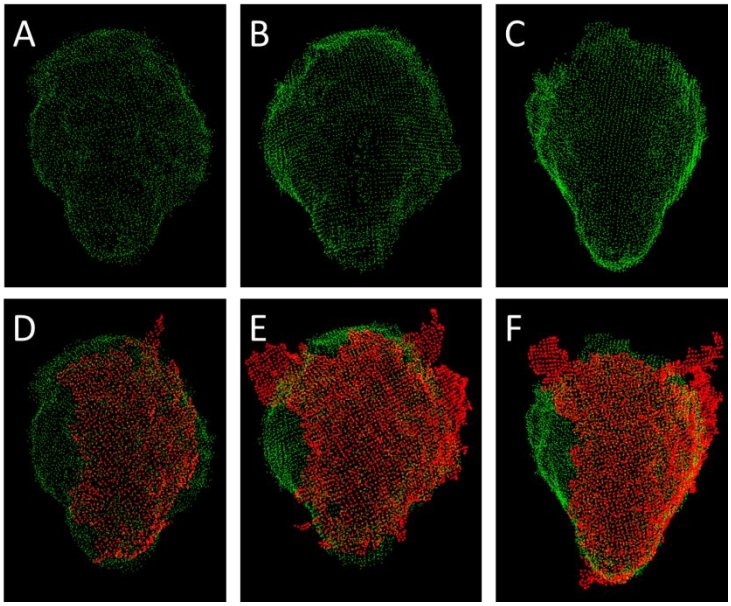

Figure 5. Point cloud models of the 3 different rat heads A) rat 1, B) rat 2 and C) rat 3). Second row one sample of a frame point cloud (red) matched with the model (green) for D) rat 1, E) rat 2 and F) rat 3.

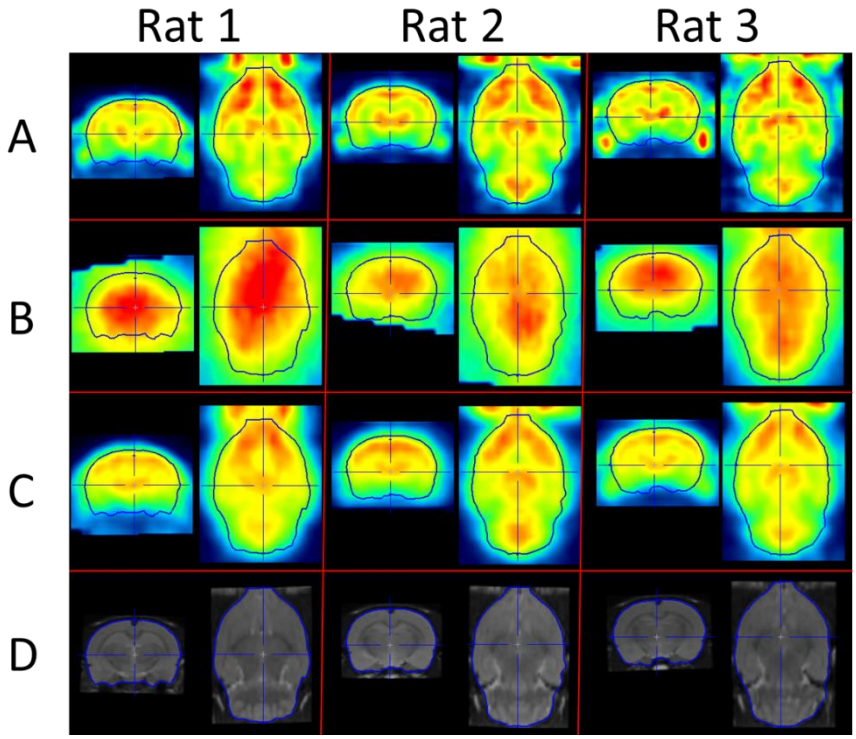

Figure 6. Coronal and axial slices of the reconstruction of the A) anesthesia scan, B) awake scan and C) awake scan after motion correction for the 3 rats. D) Magnetic resonance template of a rat brain for reference.

Figure 7 shows the Bland-Altman plots for the relative [^{18}F]FDG uptake for all 3 rats. The 95% limits of agreement have a range of 60.2 and 22.1% for the uncorrected and motion corrected images respectively.

Table 2. Correlation coefficient r between relative [18F]FDG uptake in the 22 brain regions between anesthesia and awake reconstructions and between anesthesia and awake motion corrected reconstructions. ($^{*}p$ <0.05; $^{****}p$ <0.0001).

	Rat 1	Rat 2	Rat 3
Anesthesia vs Awake	0.003	0.361	0.510 *
Anesthesia vs Awake MC	0.903 ****	0.888 ****	0.936 ****

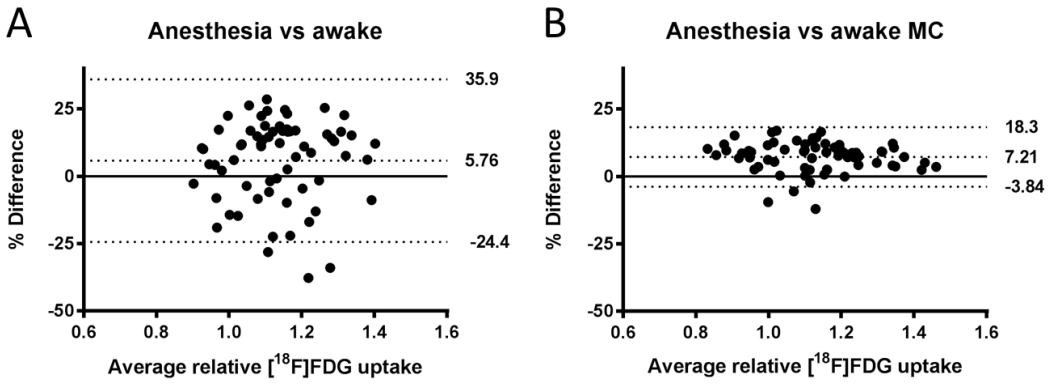

Figure 7. Bland-Altman plot for the relative [^{18}F]FDG uptake in the different brain regions A) between anesthesia and uncorrected awake scans and B) between anesthesia and motion corrected awake scans. The individual points represent one brain region for one of the 3 rats. Upper, center and lower dotted lines mark the upper 95% limit of agreement, bias and lower 95% limit of agreement of the percentage difference respectively.

The scale parameter as measured from the image correlation between Gaussian filtered anesthesia and awake motion corrected images was 1.22, 1.22 and 0.95 mm^2 for rat 1, 2 and 3 respectively. This result can be observed qualitatively in figure 5, where the hippocampus uptake pattern is less deformed in rat 3 in comparison with rat 1 and 2.

5 Discussion

Motion tracking of an awake rat head using an infrared structured light stereo camera was demonstrated using a tracking algorithm with point cloud processing techniques. The obtained motion information was then used for PET motion correction. The main advantage of this approach is that no intervention, e.g. for marker attachment, is needed when using the projected structured light stereo camera to track the motion of the rat head during the PET scan. In addition, the use of the structured light is particularly helpful when tracking the rat head as this method does not require high contrast features to be present in the imaging scene for the 3D stereo matching calculation.

The accuracy of the motion tracking influences the quality of the PET motion corrected reconstruction and depends on the performance of the ICP algorithm as well as on factors such as the camera depth resolution and optics blur which in turn depend on the focal length and on the object to camera distance.

The point clouds of objects further away from the camera have a lower depth resolution and higher noise due to the optics blur. In our experiments the camera was placed such that the distance from the camera to the tetrahedron reference was approximately at the optimal distance of 320 mm, where the optics blur of our setup was minimal. The object inside the PET scanner is further away from the camera at approximately 440 mm, causing lower depth resolution and higher noise in its point cloud. The reference tetrahedron was placed at the optimal distance as a high accuracy of the reference pose is desirable. The average standard deviation in the reference position determination was 0.035 mm and 0.170 degrees in orientation.

The oval shape of the rat head is suitable for the ICP matching. In all frames only a partial view of the rat head is seen by the camera due to the camera field of view geometry and the small PET scanner bore. Nevertheless, the partial view of the head had sufficient shape features to perform the ICP matching on the rat head model. However, when the rat head is greatly occluded the matching of the model point cloud can fail.

The presence of clutter (scene points added to the point cloud and not belonging to the object to be tracked) is another factor affecting the ICP matching accuracy. In most cases part of the rat body was included in the point cloud cluster of the head. Sometimes, although less frequently, part of the plastic cylinder holder was also included in the head point cloud. If the shape of the rat head did not change, the ICP algorithm could handle the presence of extraneous objects. However, when the clutter was severe, e.g. when the rat was grooming and its paws were included in the rat's face point cloud, the ICP matching failed. For instance, in the case of rat 1 the low tracking success rate was affected by the long grooming periods.

Lastly, the non-rigid motion of the rat face also influences the accuracy of the ICP matching. Even if the rat head is acquired in the absence of occlusion and clutter, a distorted shape can cause an incorrect pose calculation when matched with a rigid head model. The nose and mouth of the rat head are constantly moving independently of the head, although their motion is moderate. Due to the random occurrence and gentle non-rigid motion of different parts of the rat head, it is difficult to assess its influence in the pose calculation. Non rigid motion ICP algorithms exist (Li *et al.*, 2008) and alleviate

the error introduced by this kind of motion. However, these algorithms are very time consuming and were therefore not considered in this work.

The point cloud processing algorithms were run off line. This is possible in PET imaging as the raw PET data are generally stored and image reconstruction is also performed after acquisition. Execution time scales with the number of cloud points at a rate depending on the used algorithm. For this reason, the density of the point cloud determines the tracking processing time. With a point cloud sampling of 1 mm^3 the tracking processing time of a frame takes approximately 600 ms. The original denser point cloud with 0.5 mm voxel grid resolution was not used as the processing time was prohibitively long (approximately 10 s to process each frame). Further reducing the sampling size can greatly reduce the processing time, although compromising the tracking accuracy.

With all factors involved in the tracking procedure, a submillimeter tracking accuracy was achieved when measuring a static marker, with about 0.2 mm standard deviation in the position measurements and less than 1 degree in the rotation determination. However, other factors such as noise, clutter, occlusion and, in the case of the rat head experiments, non-rigid motion, affected the motion tracking of a moving object. Therefore we considered the resolution phantom and awake imaging experiments in order to assess the combined direct impact on the image quality of the motion corrected image.

The motion corrected reconstructions suffer from loss of spatial resolution in comparison with the motion-free reconstructions as is generally the case for motion corrected images (Kyme *et al.*, 2011). In the microDerenzo phantom motion corrected reconstructions, the FWHM of the rods increased on average 0.67 mm for the 2, 2.5 and 3 mm rods. In the rat experiments the spatial resolution is degraded in comparison with the motion-free reconstructions. The rat brain reconstruction in which the ICP distance score was highest (less overlap between target and source point clouds) showed greater degradation than the reconstructions with smaller distance score (greater point clouds overlap). This is also reflected in the scale parameter where the lowest value (0.95 mm^2) corresponds to the smallest distance score (0.677 mm). Nevertheless the correlation in relative uptake between anesthesia and awake scan reconstructions was greatly improved after motion correction of the awake scan reconstructions for all three cases. However it should be noted that exact agreement between the awake motion corrected reconstructions and anesthesia motion-free reconstructions is not expected, as factors such as differences in statistical noise and slight changes in tracer uptake can occur.

In clinical PET setups the use of point cloud processing for motion tracking of the human head has been investigated. In the implementation by Olesen *et al.* (2012) a near-infrared structured light projector is used. In the work by Noonan *et al.* (2015) the Microsoft Kinect has been adapted for motion tracking in PET clinical environments. The standard deviation in position measurements for their system (0.36 mm) was similar to that of our implementation (0.33 mm). Here we report on, to our knowledge, the first implementation of motion tracking using structured light for awake small animals in PET tomography. The image quality in the motion correction image was found to be similar to that obtained with implementations using marker-based tracking in small animal PET (Kyme *et al.*, 2011). A dedicated study comparing both methods could give a more quantitative comparison. However, the structured light approach offers the advantage of being less invasive.

Improvement in the motion tracking success rate and precision can be made by using several cameras to cover different views of the same object. In addition a larger bore size could enable better viewpoints for the different camera's which might improve the image quality of the motion corrected images.

6 Conclusions

Markerless motion tracking using a structured light stereo camera system and point cloud processing algorithms was effectively used to correct motion in awake rat brain PET imaging. The method allows performing awake scans of rats without the need for additional manipulations such as marker attachment. The tracking accuracy in phantom experiments showed to be sufficient for the preclinical PET scanner spatial resolution.

Acknowledgments

Authors thank Philippe Joye and Caroline Berghmans for their assistance in animal experiments. The work was supported with an UA BOF-GOA 2013 (FFB6244) grant.

References

Alexa M, Behr J, Cohen-Or D, Fleishman S, Levin D and Silva C T 2003 Computing and rendering point set surfaces *Ieee T Vis Comput Gr* **9** 3-15

Babaud J, Witkin A P, Baudin M and Duda R O 1986 Uniqueness of the gaussian kernel for scale-space filtering *IEEE Trans Pattern Anal Mach Intell* **8** 26-33

Balasse L, Maerk J, Pain F, Genoux A, Fieux S, Lefebvre F, Morel C, Gisquet-Verrier P, Laniece P and Zimmer L 2015 PIXSIC: A Wireless Intracerebral Radiosensitive Probe in Freely Moving Rats *Molecular imaging* **14** 484-9

Besl P J and Mckay N D 1992 A Method for Registration of 3-D Shapes *Ieee T Pattern Anal* **14** 239-56

EnsensoGmbH c2015 http://www.ensenso.com/manual/.

Fischler M A and Bolles R C 1981 Random Sample Consensus - a Paradigm for Model-Fitting with Applications to Image-Analysis and Automated Cartography *Commun Acm* **24** 381-95

Fueger B J, Czernin J, Hildebrandt I, Tran C, Halpern B S, Stout D, Phelps M E and Weber W A 2006 Impact of animal handling on the results of 18F-FDG PET studies in mice *Journal of nuclear medicine : official publication, Society of Nuclear Medicine* **47** 999-1006

Giavarina D 2015 Understanding Bland Altman analysis *Biochemia medica* **25** 141-51

Hildebrandt I J, Su H and Weber W A 2008 Anesthesia and other considerations for in vivo imaging of small animals *ILAR journal / National Research Council, Institute of Laboratory Animal Resources* **49** 17-26

Kyme A, Se S, Meikle S, Angelis G, Ryder W, Popovic K, Yatigammana D and Fulton R 2014 Markerless motion tracking of awake animals in positron emission tomography *IEEE transactions on medical imaging* **33** 2180-90

Kyme A Z, Zhou V W, Meikle S R, Baldock C and Fulton R R 2011 Optimised motion tracking for positron emission tomography studies of brain function in awake rats *PloS one* **6** e21727

Li H, Sumner R W and Pauly M 2008 Global correspondence optimization for non-rigid registration of depth scans *Comput Graph Forum* **27** 1421-30

Matsumura A, Mizokawa S, Tanaka M, Wada Y, Nozaki S, Nakamura F, Shiomi S, Ochi H and Watanabe Y 2003 Assessment of microPET performance in analyzing the rat brain under different types of anesthesia: comparison between quantitative data obtained with microPET and ex vivo autoradiography *NeuroImage* **20** 2040-50

Menke M, Atkins M S and Buckley K R 1996 Compensation methods for head motion detected during PET imaging *Ieee T Nucl Sci* **43** 310-7

Miranda A, Staelens S, Stroobants S and Verhaeghe J 2015 Fast motion tracking of radioactive markers for motion correction of awake and unrestrained rat brain PET *2015 IEEE Medical Imaging Conference*

Momosaki S, Hatano K, Kawasumi Y, Kato T, Hosoi R, Kobayashi K, Inoue O and Ito K 2004 Rat-PET study without anesthesia: anesthetics modify the dopamine D1 receptor binding in rat brain *Synapse* **54** 207-13

Noonan P J, Howard J, Hallett W A and Gunn R N 2015 Repurposing the Microsoft Kinect for Windows v2 for external head motion tracking for brain PET *Physics in medicine and biology* **60** 8753-66

Olesen O V, Paulsen R R, Hojgaard L, Roed B and Larsen R 2012 Motion tracking for medical imaging: a nonvisible structured light tracking approach *IEEE transactions on medical imaging* **31** 79-87

Patel V D, Lee D E, Alexoff D L, Dewey S L and Schiffer W K 2008 Imaging dopamine release with Positron Emission Tomography (PET) and (11)C-raclopride in freely moving animals *NeuroImage* **41** 1051-66

Rahmim A, Bloomfield P, Houle S, Lenox M, Michel C, Buckley K R, Ruth T J and Sossi V 2004a Motion compensation in histogram-mode and list-mode EM reconstructions: Beyond the event-driven approach *Ieee T Nucl Sci* **51** 2588-96

Rahmim A, Lenox M, Reader A J, Michel C, Burbar Z, Ruth T J and Sossi V 2004b Statistical list-mode image reconstruction for the high resolution research tomograph *Physics in medicine and biology* **49** 4239-58

Rusu R B and Cousins S 2011 3D is here: Point Cloud Library (PCL) *2011 Ieee International Conference on Robotics and Automation (Icra)*

Rusu R B, Marton Z C, Blodow N, Dolha M and Beetz M 2008 Towards 3D Point cloud based object maps for household environments *Robot Auton Syst* **56** 927-41

Schiffer W K, Mirrione M M, Biegon A, Alexoff D L, Patel V and Dewey S L 2006 Serial microPET measures of the metabolic reaction to a microdialysis probe implant *Journal of neuroscience methods* **155** 272-84

Schulz D, Southekal S, Junnarkar S S, Pratte J F, Purschke M L, Stoll S P, Ravindranath B, Maramraju S H, Krishnamoorthy S, Henn F A, O'Connor P, Woody C L, Schlyer D J and Vaska P 2011 Simultaneous assessment of rodent behavior and neurochemistry using a miniature positron emission tomograph *Nature methods* **8** 347-52

Sung K K, Jang D P, Lee S, Kim M, Lee S Y, Kim Y B, Park C W and Cho Z H 2009 Neural responses in rat brain during acute immobilization stress: a [F-18]FDG micro PET imaging study *NeuroImage* **44** 1074-80

Woody C, Vaska P, Schlyer D, Pratte J F, Junnarkar S, Park S J, Stoll S, Purschke M, Southekal S, Kriplani A, Krishnamoorthy S, Maramraju S, Lee D, Schiffer W, Dewey S, Neill J, Kandasamy A, O'Connor P, Radeka V, Fontaine R and Lecomte R 2007 Initial studies using the RatCAP conscious animal PET tomograph *Nucl Instrum Meth A* **571** 14-7

Zhou V W, Kyme A Z, Meikle S R and Fulton R 2008 An event-driven motion correction method for neurological PET studies of awake laboratory animals *Molecular imaging and biology : MIB : the official publication of the Academy of Molecular Imaging* **10** 315-24